Catalysis Today 249 (2015) 244–251

Contents lists available at ScienceDirect

Catalysis Today

journal homepage: www.elsevier.com/locate/cattod

Nitrogen-doped herringbone carbon nanofibers with large lattice spacings and abundant edges: Catalytic growth and their applications in lithium ion batteries and oxygen reduction reactions

Xin-Bing Cheng, Qiang Zhang*, Hao-Fan Wang, Gui-Li Tian, Jia-Qi Huang, Hong-Jie Peng, Meng-Qiang Zhao, Fei Wei

Beijing Key Laboratory of Green Chemical Reaction Engineering and Technology, Department of Chemical Engineering, Tsinghua University, Beijing 100084, China

ARTICLE INFO

Article history:
Received 21 August 2014
Received in revised form 29 October 2014
Accepted 30 October 2014
Available online 28 November 2014

Keywords:
Carbon nanofibers
Nitrogen doping
Lithium ion batteries
Oxygen reduction reaction
Layered double hydroxides

ABSTRACT

N-doped herringbone carbon nanofibers (N-HBCNFs) were efficiently fabricated by chemical vapor deposition on Ni nanoparticles derived from layered double hydroxide precursors. The as-obtained CNFs were with an average diameter of ~60 nm, a high purity of ~91.6%, and a large specific surface area of 108.1 $m^2 g^{-1}$. When employed as anode materials, the N-HBCNFs yielded a reversible capacity of 500.0 mAh g^{-1} at a current density of 0.10 C (1.0 C = 372 mA g^{-1}) and rapid lithium storage properties with a high capacity of 141.6 mAh g^{-1} at 5.0 C. When the N-HBCNFs were used as catalyst for oxygen reduction reaction, an onset potential of 0.85 V, an electron transfer number of 3.1, and a current retention of 69.1% after 16,000 s test were detected, indicating the good reactivity of N-HBCNF catalyst for electrocatalysis application. The superior performance of N-HBCNFs was attributed to their enlarged graphitic lattice spacings and abundant edges on the surface, which afforded more active sites for both Li ion storage and oxygen reduction reaction. Thus, the N-HBCNFs are promising nanocarbon materials for various applications in lithium ion batteries, lithium-sulfur batteries, lithium-air batteries, fuel cells, and so on.

1. Introduction

Energy storage systems represented by rechargeable batteries and fuel cells are receiving increasing attention, as their applications are successively expanding from small-scale mobile electronics to large-scale transportations and utility grids [1–5]. The nanostructured carbon is one of the core materials for high performance energy storage devices [1,3,5]. The intensive investigations of nanocarbons, especially the highly conductive sp^2 carbon, shed a light on the improvement of the conductive nature and thus efficient utilization of the electrodes [5,6] and boosting the researches of next-generation energy storage systems.

Well arrangement of sp^2 carbon layers renders one-dimensional (1D) carbon nanotubes (CNTs) or carbon nanofibers (CNFs), two-dimensional (2D) graphene nanosheets, and three-dimensional (3D) nanostructured carbon with unexpected properties for vast applications in heterogeneous catalysis [7–10] and energy storage [1,5,11,12]. The key issue for the successful applications of nanocarbon lies in the ability to pack the sp^2 carbon layers into the desired 3D structures. Among these materials, the herringbone CNFs (HBCNFs) are one kind of promising nanocarbons [13] for rechargeable batteries due to their cavities, open tips, and graphite platelets, which may provide more active sites and enhance the utilization rate of active materials in the composite electrodes.

Another approach to improve the electrochemical performance for the carbon-based electrode is to modify its surface functional groups by non-carbon element doping [14–16]. The presence of heteroatoms at the carbon surface enhance the reactivity and electric conductivity [10,14,15,17], and hence the energy storage capacity [14]. Consequently, the chemical properties of HBCNFs can be tailored by heteroatom functionalization on nanocarbon sheets or molecular carbon geometries at the edges, defects, or strained regions. A particularly exciting example is the nitrogen (N)-doped carbon nanosheet that bears five valence electrons. A shift in the Fermi level to the conducting band is presented when N is doped in carbon lattice as electron donors. With the incorporation of N into the carbon framework, the activity of HBCNFs for oxygen reduction [18,19] or lithium ion storage [20] is expected to be significantly

* Corresponding author. Tel.: +86 10 62794136; fax: +86 10 62772051.
E-mail address: zhang-qiang@mails.tsinghua.edu.cn (Q. Zhang).

http://dx.doi.org/10.1016/j.cattod.2014.10.047
0920-5861/

improved. The promising behaviour of N-doped HBCNFs is due to the introduction of additional n-type carriers in carbon systems and the hybridization between the nitrogen lone pair electrons and the carbon π-electron system [21]. Thus, exploring N-doped nanocarbons with controllable doping manner and tailored microstructures is scientifically necessary to demonstrate the material chemistry and potential applications of N-doped HBCNFs (N-HBCNFs), as well as to allow mechanistic insight into the roles that heteroatoms played on their textures and activities. Furthermore, N-HBCNFs are expected to be a promising material in electrochemical energy storage and metal-free catalysis (e.g. oxygen reduction reaction (ORR) in fuel cells and lithium-oxygen (Li-O_2) batteries) [18,19].

In this contribution, N-HBCNFs were efficiently fabricated by catalytic chemical vapor deposition (CVD) of C_2H_4 and NH_3 on Ni nanoparticles derived from layered double hydroxide (LDH) precursors at 600 °C. Electrochemical measurements demonstrated that N-HBCNFs presented a higher specific capacity and excellent rate performance, as well as cycling stability when compared with HBCNFs and CNTs. N-HBCNFs also exhibited great potential to serve as an anode material in lithium ion batteries and nanocarbon based catalysts for ORR.

2. Experimental

2.1. Catalyst preparation

The Ni based LDH catalysts were synthesized through the co-precipitation reaction by adding urea into aqueous solution of nickel nitrate and aluminum nitrate similar to our previous reports [22,23]. In detail, both $Ni(NO_3)_2{\cdot}6H_2O$ and $Al(NO_3)_3{\cdot}9H_2O$ were dissolved in 250 mL deionized water with $[Ni^{2+}] + [Al^{3+}] = 0.15\ mol\ L^{-1}$ (n(Ni): n(Al) = 3: 1). The urea was then dissolved in the solution with [urea] = 3.0 mol L^{-1}. The as-obtained solution was kept at 100 °C under continuous magnetic stirring (equipped with a reflux condenser in ambient atmosphere) for 9.0 h in a 500.0 mL flask, and then at 94 °C for another 12.0 h with the stirring off. After several steps of filtering, washing, and freeze-drying, the final products of Ni/Al LDH catalyst precursors were available for N-HBCNF growth.

2.2. Catalytic growth of N-HBCNFs

The N-HBCNFs were synthesized over Ni/Al LDH derived catalysts with C_2H_4 and NH_3 as carbon and nitrogen sources, respectively. A fixed-bed reactor was used for nanocarbon deposition. During the catalytic deposition, the reactor was heated to 900 °C at a heating rate of 20 °C min^{-1} in Ar (100 mL min^{-1}). Then, the LDHs were reduced by H_2 (100 mL min^{-1}) for catalyst nucleation into large active Ni particles with well defined crystal surfaces for N-HBCNF deposition. After that, H_2 was stopped and the reduced catalysts were cooled down to 600 °C to synthesize CNFs in $C_2H_4/NH_3/Ar$ (100/100/100 mL min^{-1}). Finally, the reactor was cooled down under Ar atmosphere. The HBCNFs were obtained with the same route except the feedstocks were solely C_2H_4 instead of C_2H_4/NH_3 mixture.

The as-grown products were treated by NaOH (12.0 mol L^{-1}) aqueous solution at 150 °C for 6.0 h and subsequent HCl (5.0 mol L^{-1}) aqueous solution at 80 °C for 3.0 h to remove the residual catalysts. The N-HBCNFs with high carbon purity were fabricated after filtering, washing, and freeze-drying.

2.3. Characterization

The CNF products were characterized by a JSM 7401F scanning electron microscope (SEM) and a JEM 2010 high-resolution transmission electron microscope (TEM). The level of CNF graphitization was determined by X-ray diffraction (XRD) on a Bruker D8 Advance diffractometer at 40.0 kV and 120 mA with Cu K_α radiation. Raman spectra were collected on a Horiba Jobin Yvon LabRAM HR800 Raman spectrophotometer. TG analysis was operated by Mettler Toledo TGA/DSC-1 to calculate the purities of CNFs. The N_2 adsorption–desorption isotherms were obtained using an N_2 adsorption analyzer (Autosorb-IQ_2-MP-C system). The specific surface area of all samples was calculated by BET method. The pore size distribution plots were obtained by the non-linear density functional theory method.

2.4. Li-ion storage performance of N-HBCNFs

The Li-ion storage performance of N-HBCNFs was evaluated in a routine two-electrode cell configuration using standard 2025 coin-type cells. A homogeneously slurry was prepared by mixing N-HBCNFs and polyvinylidene difluoride (PVDF) binder in N-methylpyrrolidinone with a mass ratio of N-HBCNFs: PVDF = 9: 1, followed by magnetic stirring for ca. 24.0 h. The areal loading amount of N-HBCNFs was ca. 1.8 mg cm^{-2}. The slurry was then coated onto a Cu foil and dried in a vacuum drying oven at 60 °C for 6.0 h. The as-obtained foil was punched into 13 mm disks as the working electrodes. 1.0 mm-thick Li metal foil was employed as the counter electrode. An electrolyte of $LiPF_6$ (1.0 M) in a mixed solution of ethylene carbonate-dimethyl carbonate-ethylene methyl carbonate with a mass ratio of 1:1:1 was used. A microporous Celgard 2400 membrane was used as the separator. The assembling of cells was conducted in an Ar-filled glove box with oxygen and water content below 1 ppm. The coin cells were tested in the galvanostatic mode within a voltage range of 0.01–1.5 V using Neware multichannel battery cycler. The cyclic voltammogram (CV) measurements were performed on a Solartron 1470E electrochemical workstation at a scan rate of 0.10 mV s^{-1}. The CNT and HBCNF electrodes were obtained with the same methods. In addition, to maximize the electrochemical performance of N-HBCNFs, CNTs were added as the conductive agents in the long cycling test.

2.5. ORR performance of N-HBCNFs

The as-purified N-HBCNF samples were firstly dispersed in ethanol (5.0 mg mL^{-1}) by sonication. 10 μL N-HBCNF suspension was pipetted onto the glass carbon disk electrode surface, which was polished mechanically with 0.05 μm alumina slurry and then washed with deionized water and acetone to obtain a mirror-like clean surface prior to use. After solvent evaporation for 10 min in air, a thin layer of Nafion solution (1.0 wt%) was coated onto the electrode surface and then dried in an oven at 60 °C for 30 min before measurement.

The electrochemical measurements were conducted on a rotating ring-disk electrodes (RRDE) configuration (Pine Research Instrument, USA) in a three-electrode electrochemical cell using a computer-controlled potential station (CHI 760D, CH Instrument, USA). A rotating ring disk electrode with a disk diameter of 5.0 mm served as the substrate for the working electrode. A saturated calomel electrode (SCE) and Pt foil electrode were used as the reference and counter electrode, respectively. The oxygen reduction tests were carried out in O_2-saturated 0.10 mol L^{-1} KOH solution at room temperature. The disk electrode was scanned cathodically at a rate of 5.0 mV s^{-1} in the potential range of 0.2 to −0.8 V vs. SCE and the ring potential was set constant at + 0.5 V vs. SCE to monitor the formation of peroxide intermediate. The electron transfer number n and HO_2^- intermediate production percentage (%HO_2^-) were calculated based on the disk and ring current as followed:

$$n = \frac{4I_d}{I_d + I_r/N} \quad (1)$$

$$\%HO_2^- = 100(2/n)\text{-}50 \quad (2)$$

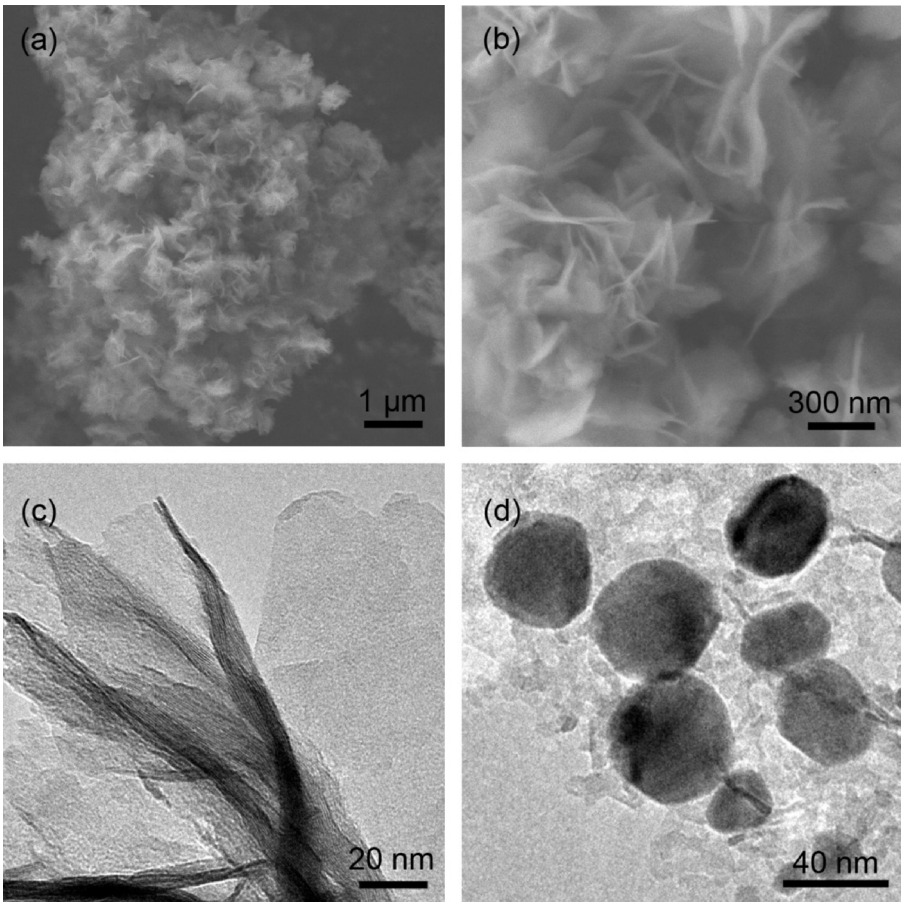

Fig. 1. LDH based catalysts for N-HBCNF formation: (a) The low and (b) high magnification SEM images of the NiAl LDH flakes; the TEM images of (c) LDH flakes and (d) reduced LDO catalysts for the N-HBCNF growth.

where I_d is disk current, I_r is ring current and N is current collection efficiency of the Pt ring which was determined as 0.26.

3. Results and discussion

3.1. N-HBCNFs synthesized from Ni/Al LDH derived catalysts

The Ni/Al LDHs were employed as the catalyst precursors for catalytic growth of HBCNFs and N-HBCNFs. LDHs are a class of synthetic two-dimensional nanostructured anionic clays, in which most metals (such as Mg, Al, Fe, Co, Ni, Cu, etc.) can be dispersed *at an atomic scale* with controllable components [24,25]. After reduction, embedded metal particles with highly controllable density and particle size were available for the controllable synthesis of CNTs and CNFs [26,27]. Herein, a large amount of Ni/Al LDH agglomerates served as the substrates and catalyst precursors. The typical morphology of the as-prepared Ni/Al LDHs is shown in Fig. 1a–c. The LDH flakes were agglomerated into a flower-like shape, winding around a core with the size of 95 and 450 nm for the "flower" and the "petal", respectively. The LDHs were very fluffy and with a low packing density of approximately 200 kg m^{-3}. The Ni/Al LDH flakes were firstly calcined into layered double oxide (LDO) flakes during the heating process, which transformed the initial structure of LDH precursor into monolithic structured Ni/Al LDO (Fig. 1d). Ni NPs with a size of 20–40 nm and a high density of ca. 3×10^{11} cm^{-2} were distributed on the calcined LDO flakes after the reduction in H_2 atmosphere. With the introduction of C_2H_4 and NH_3, N-HBCNFs were grown on the reduced NiAl LDO flakes.

The N-HBCNFs were entangled with each other and grown in random directions (Fig. 2a), leading to a closely agglomerated nanostructure. The average diameter of the N-HBCNFs was measured as 60 nm (Fig. 2b). N-HBCNFs are with quite different morphology of routine CNTs or a similar structure with HBCNFs grown from the same Ni/Al LDH precursor (Fig. S1). The angle between the orientation of graphitic layers and the *c*-axis of the as-grown N-HBCNFs was 29.2°. The layer spacing between the graphitic layers of the N-HBCNFs was around 0.345 nm (Fig. 2c), which was slightly larger than that of ideal graphite (0.335 nm) and HBCNFs (0.341 nm). This was expected to render a much faster ion transfer between the graphitic layers. The size of sp^2 domains in the N-HBCNFs was estimated to be 10–40 nm. Such sp^2 domains were cup-stacked with each other. The edges of graphene nanosheets were directly exposed to the outer wall of the CNFs. The introduction nitrogen heteroatoms induced more defects to facilitate the lithium ion storage.

A sharp loss of mass to 8.36% was observed in the TG profile of the N-HBCNF sample (Fig. S2) between a temperature window from 390 to 451 °C, which was much lower than that of HBCNFs (450–515 °C). This indicated the introduction of nitrogen atoms into the HBCNFs significantly reduced their thermal stability. The purity of raw N-HBCNFs was 91.6%, indicating a high carbon yield of ca. 11 $g_{N\text{-}HBCNF}/g_{cat}$. This was significantly higher than that of single-walled (~0.001–1 g_{CNT}/g_{cat}) [28] and double-walled (~0.01–2 g_{CNT}/g_{cat}) CNTs [29] grown on LDH-based catalysts. The high carbon yield was attributed to the high reactivity of CNF formation on the Ni based catalyst, enough space for CNF formation, as well as long life span of Ni based catalysts. A very sharp and strong

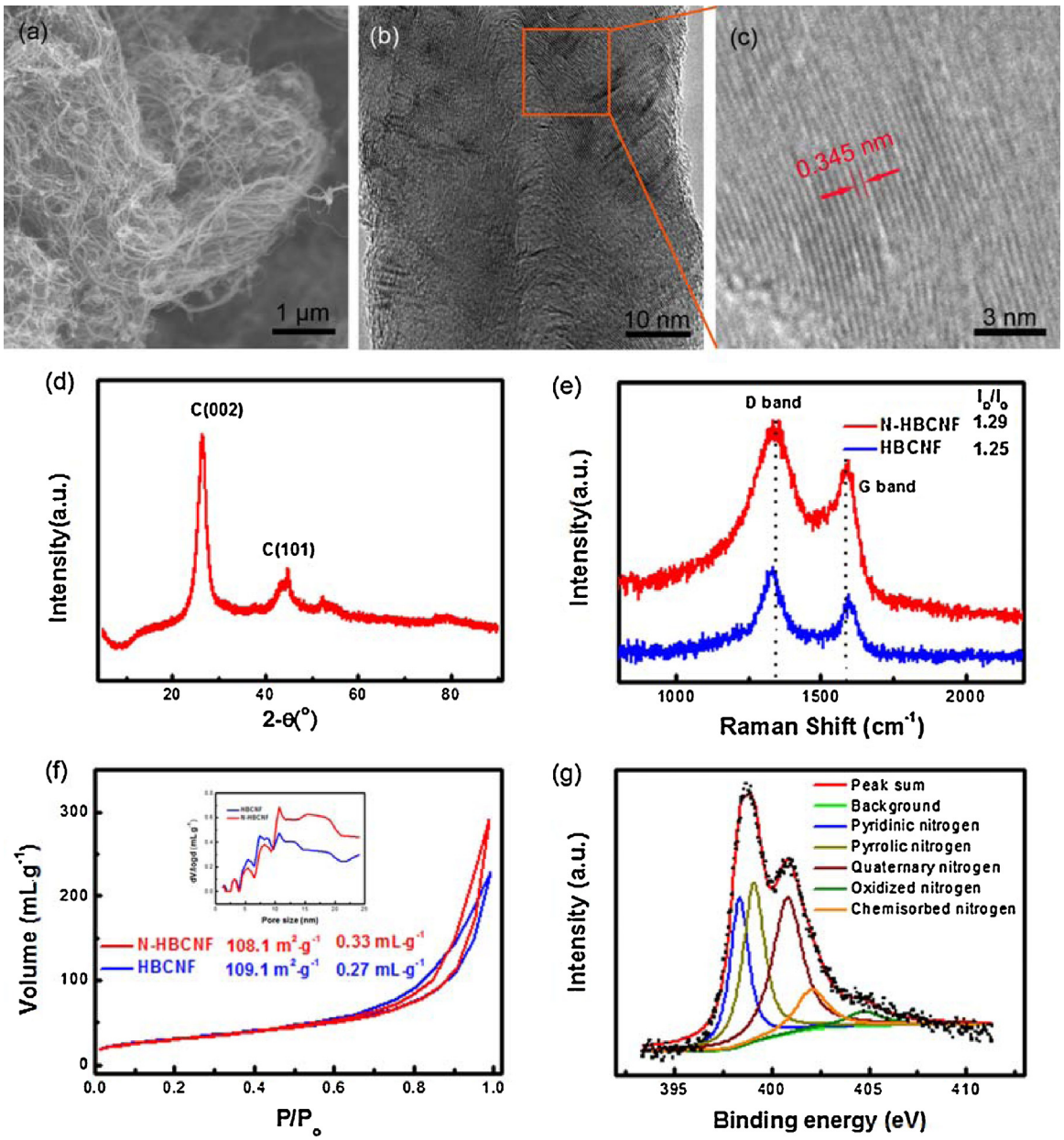

Fig. 2. The morphology and microstructures of N-HBCNFs: (a) SEM image, (b) low and (c) high magnification TEM images of N-HBCNFs; (d) The XRD pattern of the N-HBCNFs, (e) Raman spectra and (f) N_2 isothermal adsorption and desorption curves of HBCNFs and N-HBCNFs, inset shows the corresponding pore size distribution, (g) XPS spectra in N region of the obtained N-HBCNFs.

(0 0 2) diffraction peak was detected on the XRD pattern of the as-obtained N-HBCNFs (Fig. 2d). Fig. 2e exhibited the Raman spectra of the HBCNFs and N-HBCNFs. Both the in-plane vibration of graphitic lattice (G band at 1575 cm^{-1}) and the disorder band aroused from amorphous carbon and edges (D band at 1350 cm^{-1}) were identified. The I_D/I_G ratio was employed to evaluate the defect degree of the graphene nanosheets. The values of I_D/I_G for the as-grown HBCNFs and N-HBCNFs were 1.25 and 1.29, respectively, indicating a larger amount of defects in N-HBCNF products induced by the nitrogen doping. The N_2 isothermal adsorption and desorption curves and their corresponding pore size distributions of the HBCNFs and N-HBCNFs were shown in Fig. 2f. The BET specific surface areas were determined to be 109.2 and 108.1 $m^2\ g^{-1}$, respectively.

The XPS spectra of the nitrogen region in Fig. 2g revealed the relative proportions of different N-containing functional groups. The relative ratios of pyridinic nitrogen (398.4 eV), pyrrolic nitrogen (399.1 eV), quaternary nitrogen (400.8 eV), chemisorbed nitrogen (404.7 eV), and oxidized nitrogen (402.1 eV) were 22.8, 28.4, 33.6, 4.4, and 10.8%, respectively. Note that pyrrolic nitrogen and pyridinic nitrogen dopants were located at the edge or surface "hole" defect sites in N-HBCNFs. The nitrogen doping level was 5.15 atom% (Table 1), which was similar to that of nanocarbon from CVD of hydrocarbon/NH_3 mixture [30–33]. The N doping induced excess electrons and more defects in the outer layer and enlarged distances of graphite interlayer, which favored lithium-ion storage and transfer. This rendered an improved performance relative to pristine HBCNFs and CNTs.

3.2. Li-ion storage performance of the N-HBCNFs

Li-ion batteries were applied to investigate the effect of N doping on the ion diffusion rate. The electrochemical performances

Table 1
Summary of nitrogen species in N-HBCNF products.

Sample	Total content of nitrogen (at.%)	Relative amounts of nitrogen species (at.%)				
		Pyridinic nitrogen (398.4 eV)	Pyrrolic nitrogen (399.1 eV)	Quaternary nitrogen (400.8 eV)	Chemisorbed nitrogen (404.7 eV)	Oxidized nitrogen (402.1 eV)
N-HBCNF	5.15	22.8	28.4	33.6	4.4	10.8

of CNTs, HBCNFs, and N-HBCNFs were evaluated with 2025-type coin half-cells. N-HBCNF electrode exhibited rapid lithium-ion storage property, as illustrated in Fig. 3a. The N-HBCNFs yielded a discharging capacity of 287.5, 237.4, 212.4, 196.2, 175.0, and 141.6 mAh g^{-1} at a current density of 0.1, 0.2, 0.5, 1.0, 2.0, and 5.0 C (1.0 C = 372 mA g^{-1}), respectively. This was significantly higher than those of CNT and HBCNF electrodes reported in this research. The aligned CNTs synthesized by an aerosol-assistant CVD with a diameter of 50–70 nm, a nitrogen content of 2.89 at.% exhibited a reversible capacity of 201 mAh g^{-1} at a current density of 0.2 mA cm^{-2} (Corresponding to 0.28 C in this research) [15]; The nitrogen-doped CNF webs with a high nitrogen content of 15.0 wt.% afforded a capacity of 245 mAh g^{-1} at 1.0 C [34]. The high rate capability of N-HBCNFs reported herein was attributed to the loose packing of graphene nanosheets and defects. The enlarged and tilted graphitic layers induced by nitrogen atoms prompted rapid Li-ion diffusion. The initial coulombic efficacy of N-HBCNFs, HBCNFs, and CNTs were 60.0, 39.7, and 27.4%, respectively. The large irreversible capacities of CNTs were resulted from the huge specific surface area, which exhausted a plenty of Li-ions in the formation of the solid electrolyte interphase (SEI) in the anode. Consequently, the N-HBCNFs exhibited a superior Li^+ storage performance with quite higher coulombic efficiency relative to HBCNFs due to their excellent electrical conductivity, short sp^2 carbon domains, and relatively low surface area. The charge–discharge curves of CNTs, HBCNFs, N-HBCNFs were displayed in Fig. S3. Except for the first cycle, all the anode materials employed herein exhibited a stable charge–discharge performance. However, there was no distinct platform in the voltage profiles during the discharging process. Note that we did not employ any other conductive agents in the rate performance test. The cycle performance of N-HBCNFs at a current density of 0.1 C was shown in Fig. S4 with CNTs as the conductive agents. Stable and reversible capacities of 500 mAh g^{-1} were obtained for N-HBCNF anode, which indicated that N-HBCNFs were with more active sites for Li ion storage. The long cycle performance at a current density of 0.5 C in Fig. 3b also indicated an excellent cycling stability.

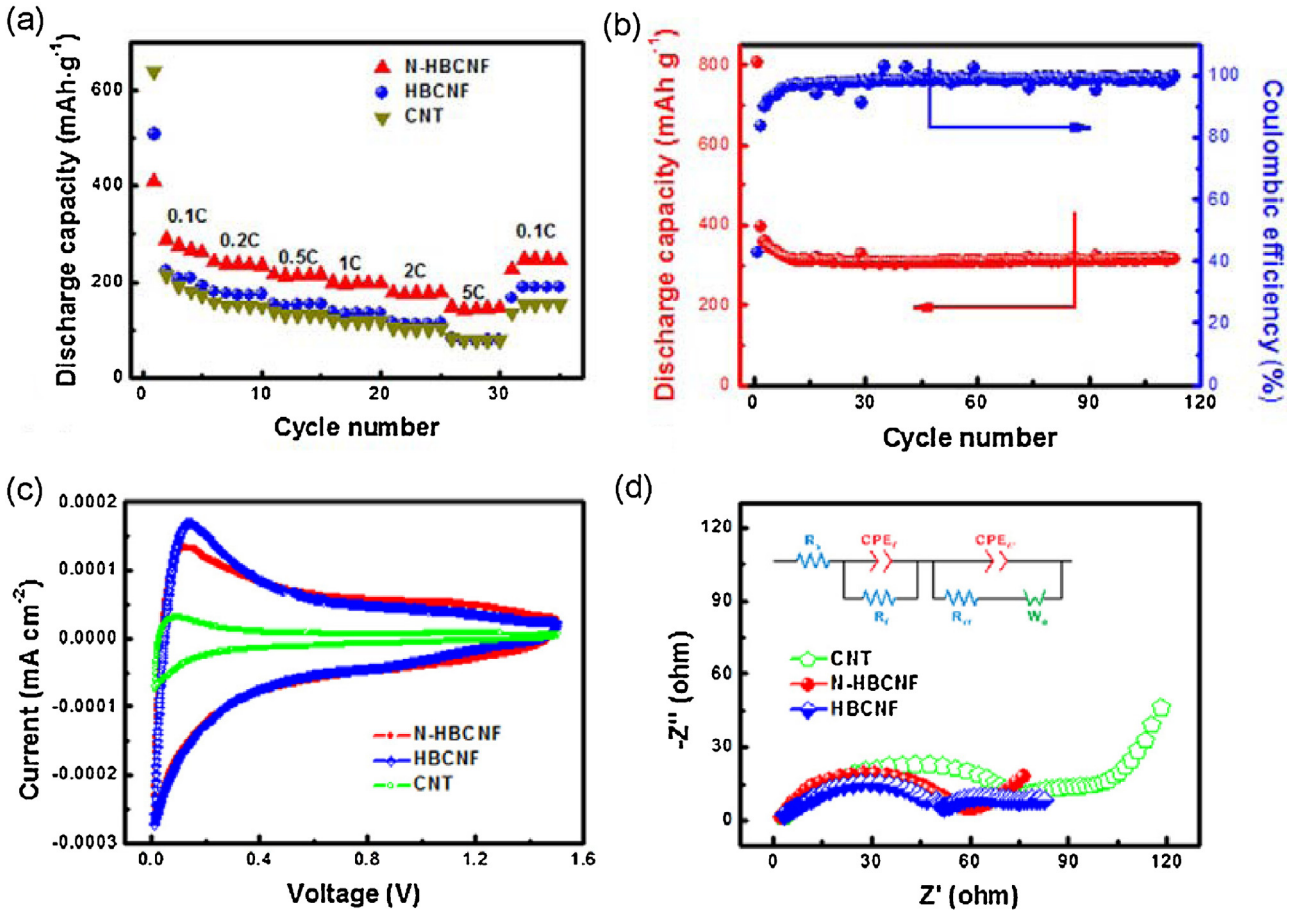

Fig. 3. Li ion storage performance of N-HBCNFs: (a) The charge/discharge performance of CNT, HBCNF, N-HBCNF anodes at different current densities (1.0 C = 372 mA g^{-1}) and (b) the cyclic performance of N-HBCNF electrode with the current of 0.5 C, (c) the cyclic voltammetry curves of N-HBCNF, HBCNF, CNT anodes at a scan rate of 0.1 mV s^{-1}, (d) the EIS spectra of CNT, HBCNF, N-HBCNF anode before cycles.

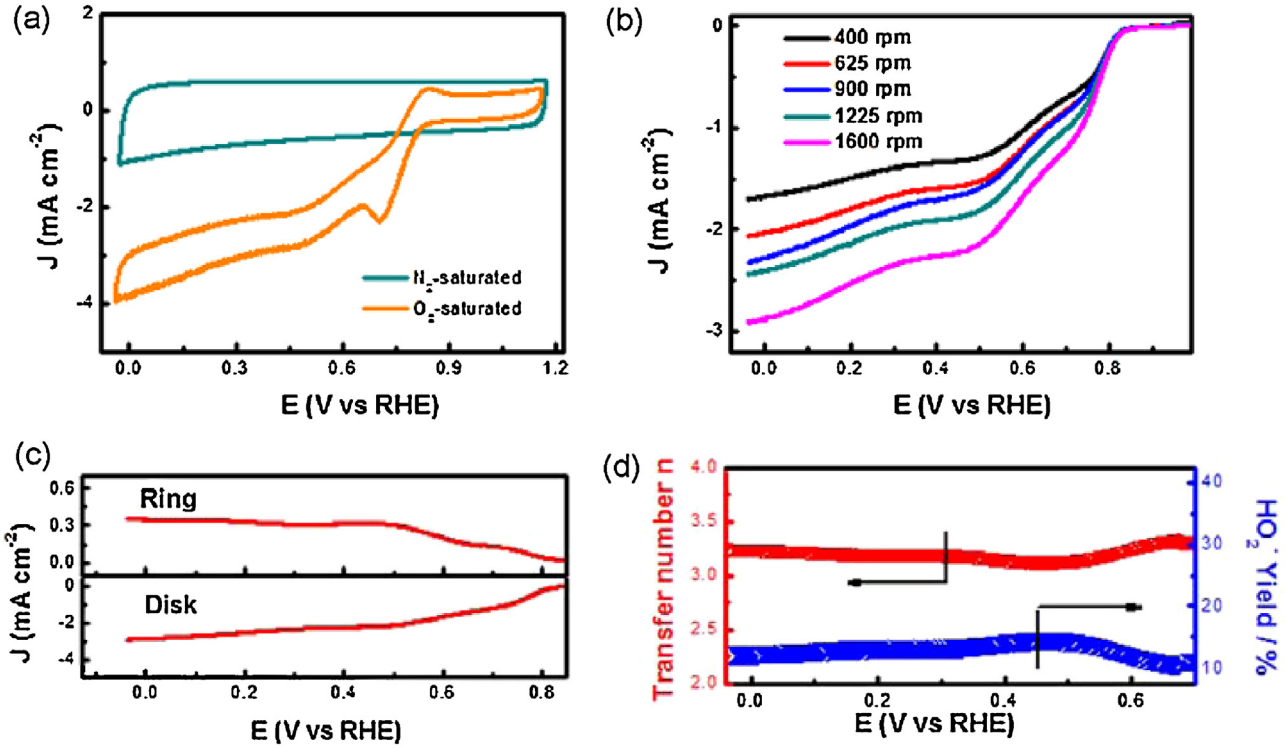

Fig. 4. The ORR performance of N-HBCNFs: (a) CV profiles of the N-HBCNFs on a glassy-carbon RDE electrode in an O_2-saturated or N_2-saturated 0.10 mol L^{-1} KOH solution. (b) Rotating-disk voltammograms recorded for N-HBCNF supported on a GC electrode in an O_2-saturated 0.10 mol L^{-1} KOH solution at a scan rate of 10 mV s^{-1} with different rotating rates. (c) Disk current densities (bottom) and the corresponding ring current densities (top) of N-HBCNF on RRDE with a consistent rotating rate of 1600 rpm in O_2-saturated 0.10 mol L^{-1} KOH solution. (d) The electron transfer number and percentage of peroxide of the hybrid catalysts at various potentials.

CV profile was used to analyze the Li-ion storage behavior. Fig. 3c showed typical CVs for CNTs, HBCNFs, and N-HBCNFs at a sweep rate of 0.1 mV s^{-1}. There were two sharp reduction/oxidation peaks at ~0.011 and 0.112 V for N-HBCNFs, which was similar to that of HBCNFs (~0.011 and 0.137 V). The reduction/oxidation peaks in CV curves were attributed to the lithium-ion insertion/extraction processes into/from graphitic layers, respectively. However, the electrochemical insertion/extraction behavior of lithium ions on CNTs was clearly different from those with tilted graphitic layers. A broad peak occurred between 0.011 and 0.089 V on the CV profile for CNT anode.

To confirm the excellent lithium-ion storage performance of N-HBCNFs, the electrochemical impedance spectra (EIS) were conducted (Fig. 3d). All the EIS profiles exhibited one or two semicircles and one linear region, in agreement with typical reaction processes [35]. The parameters in the model were extracted by fitting the EIS data with ZView software (Table 2). The R_s and R_{ct} for N-HBCNF anode were 1.79 and 36.48 Ω, which was less than 1.82 and 55.67 Ω for HBCNFs, respectively. The decrease in the charge transfer resistance indicated that the electron distribution induced by nitrogen doping on the surface of HBCNFs promoted the charge shuttle between the electrodes. However, the N-HBCNF anode was with an R_f of 22.32 Ω, which was slightly larger than that of pristine HBCNF anode. This was related with the formation of a stable SEI between the electrolyte and N-doping electrodes, which afforded positive contribution to high and stable lithium-ion storage performance. The N-doping also led to a reduced Warburg impedance from 0.097 to 0.054 Ω $s^{0.5}$, which can be attributed to the enlarged graphitic layer distance from 0.341 to 0.345 nm for HBCNFs and N-HBCNFs, respectively.

The introduction of nitrogen atoms into the carbon frameworks brings additional n-type carriers and hybridization between the nitrogen lone pair electrons and the carbon π-electron system [21]. The intrinsic property of carbon is therefore modulated, which facilitated the Li ion storage when the doped carbon materials were employed as anode materials. Some N-doped carbon materials, such as nitrogen-doped graphene nanosheets [14], CNTs [36], CNFs [37], graphene/CNT hybrids [38], porous carbon [39], exhibited improved Li ion storage performance. In this contribution, the excellent discharge capacity and rate capability of N-HBCNT anode were also detected. The 3D entangled CNFs were applied as electron pathway, while the abundant pores were served as reservoirs and transport channels for Li ions. The herringbone structure of CNFs significantly reduced the transport distance of lithium ions, while the nanopores provide interconnected channels for Li ion diffusion [22,37,40]. The introduction of nitrogen heteroatoms into the frameworks enlarged the lattice spacing among graphitic sheets, reduced the charge transfer resistance, improved the electrode/electrolyte wettability [14,17,20,41], and built a stable SEI film between the electrolyte and electrodes. The stronger electronegativity of nitrogen compared to carbon can increase the adsorption energy of Li^+ ion and decrease energy barrier for Li^+ penetration [42,43]. Consequently, the N-HBCNF anode exhibited a superior lithium-ion storage performance, making it a promising anode for the Li-ion batteries. The highly exposed carbon edge and nitrogen doping level afford strong coupled interfaces between N-HBCNF with other active phases (e.g. polysulfides) [44], which is promising for their broad applications in lithium-sulfur batteries and other energy storage systems.

3.3. ORR activity of the N-HBCNF electrocatalysts

Carbon-supported platinum (Pt) and/or platinum alloys are widely accepted as electrocatalysts [45] in proton-exchange

membrane fuel cells and metal-air batteries. However, in the context of a strong economy, Pt is too expensive, hence hindering the large scale commercialization of these clean and efficient electrical energy sources. The exploration of noble-metal-free catalyst for ORR is strongly considered [46]. Very recently, nitrogen-doped carbon nanomaterials were used as an efficient ORR catalyst [19,47]. Herein, the N-HBCNFs with excellent electronic conductivity, small sp^2 carbon domains were also explored as the electrocatalyst for ORR.

Fig. 4a presented the CV profiles of N-HBCNF supported glassy carbon electrodes in 0.1 mol L^{-1} KOH solution saturated with N_2 or O_2 at a scan rate of 100 mV s^{-1}. In the N_2-saturated solution, featureless voltammetry currents within the potential range between −0.03 and +1.17 V can be observed. In contrast, the N-HBCNF electrodes demonstrated well-defined cathodic peaks for O_2 reduction when the electrolyte solution was saturated with O_2. The linear sweep voltammetry profiles (Fig. 4b) indicated that the current density was enhanced by increasing the rotating rate. The onset potential of N-HBCNF electrode for ORR was approximately 0.85 V, close to that identified from the CV measurements (0.82 V). The corresponding Koutecky-Levich equations were calculated to analyze the kinetic parameters for ORR process. Take 0.45 V for an example, the electron transfer number of N-HBCNF electrode based on the slope of the K–L plots (J^{-1} vs. $\omega^{-1/2}$) was 3.1 (Fig. S5). The RRDE technique was applied to further verify the ORR pathway and to determine the HO_2^- generation rate. Fig. 4c exhibited the profiles of current densities verses the potential at the disk and ring electrode. The corresponding charge transfer number and HO_2^- yield were shown in Fig. 4d. The amount of HO_2^- yield was ca. 14.3% at 0.45 V and the calculated *n* value was 3.1, which was in accordance with the result through Koutecky-Levich method. The electron transfer numbers of N-HBCNF is competitive with the nitrogen doped graphene-CNT hybrids (3.22) [48], nitrogen doped aligned CNTs (2.76–3.20) [49], nitrogen/sulfur co-doped graphene [50], and less than the nitrogen doped CNF aerogel derived from bacterial cellulose (3.9) [51]. The adsorbed oxygen molecule absorbed on N-HBCNF electrode preferred to obtain $4e^-$ to release OH^- during ORR. Additionally, chronoamperometric durability tests were also performed at a constant voltage of 0.67 V in a 0.1 mol L^{-1} KOH solution saturated with O_2 at a rotating rate of 1600 rpm (Fig. S6). Remarkably, continuous O_2 reduction on the N-HBCNF electrode resulted high relative current of 69.1% still persisting after 16,000 s.

It is widely accepted that the presence of nitrogen containing functional groups is necessary for the reactivity of ORR. Compared with graphene, CNT, or other sp^2 carbon, the HBCNFs reported herein is not with the highest electrical conductivity. However, the ORR performance of N-HBCNFs is still competitive with nitrogen doped graphene-CNT hybrids [48], nitrogen doped aligned CNTs [49], nitrogen/sulfur co-doped graphene [50] reported recently. This is attributed from the unique architecture of N-HBCNFs that afford continuous pathways for charge transport as well as more interconnected pores for fast mass transport. The controllable doping of nitrogen atoms not only introduced more active sites for metal–catalyst free sites [19,47,48,52,53], but also exhibited more exposed graphene edges, enlarged graphitic layer distance, as well as improved hydrophilicity of the doped carbon surface. Therefore, the electrolytes and dissolved oxygen feedstock can easily access catalytically active sites for facile oxygen reduction [54]. The full exposure of active site on the surface through coaxial nanocables [55] is a promising way to enhance the electrochemical reaction. The N-HBCNFs is expected as a novel doped sp^2 carbon platform for noble-metal-free electrocatalyst with superior reactivity and stability.

4. Conclusions

The Ni based LDHs were used as catalyst precursors for catalytic growth of N-HBCNFs by CVD with C_2H_4/NH_3 mixture as sources. The as-obtained N-HBCNFs were with a high purity (~91.6%), an average outer diameter of ca. 60 nm, a specific surface area of 108.1 $m^2 \cdot g^{-1}$, as well as a weight loss peak between 390 and 451 °C. The enlarged graphitic layer distance (0.345 nm) and defects (I_D/I_G ratio of 1.29) on the surface of N-HBCNFs induced well exposure of active sites for Li ion storage and ORR. Therefore, a high reversible capacity of 500 mAh g^{-1} at the current density of 0.10 C and fast lithium storage property with a capacity of 141.6 mAh g^{-1} at 5.0 C can be achieved, which was a significant improvement compared with pristine HBCNFs. Furthermore, the N-HBCNFs exhibited an onset potential of 0.85 V, an electron transfer number of 3.1, as well as a current retention of 69.1% after 16,000 s test for ORR. The good electrochemical performance of Li ion storage and ORR was attributed from the unique architecture of N-HBCNFs which afforded good electrical conductivity for charge transport as well as more interconnected pores for rapid mass transport. This work shed a light on the controllable doping and tailoring nanocarbon towards full exposure of active sites for electrochemical energy storage.

Acknowledgements

This work was supported by National Basic Research Program of China (973 Program, 2011CB932602) and Natural Scientific Foundation of China (No. 21422604).

Appendix A. Supplementary data

Supplementary material related to this article can be found, in the online version, at http://dx.doi.org/10.1016/j.cattod.2014.10.047.

References

[1] D.S. Su, R. Schlogl, Nanostructured carbon and carbon nanocomposites for electrochemical energy storage applications, ChemSusChem 3 (2010) 136.
[2] D.W. Wang, D.S. Su, Heterogeneous nanocarbon materials for oxygen reduction reaction, Energy Environ. Sci. 7 (2014) 576.
[3] Z.Q. Zhu, S.W. Wang, J. Du, Q. Jin, T.R. Zhang, F.Y. Cheng, J. Chen, Ultrasmall Sn nanoparticles embedded in nitrogen-doped porous carbon as high-performance anode for lithium-ion batteries, Nano Lett. 14 (2014) 153.
[4] B.J. Landi, M.J. Ganter, C.D. Cress, R.A. DiLeo, R.P. Raffaelle, Carbon nanotubes for lithium ion batteries, Energy Environ. Sci. 2 (2009) 638.
[5] D.S. Su, G. Centi, A perspective on carbon materials for future energy application, J. Energy Chem. 22 (2013) 151.
[6] Q. Zhang, J.Q. Huang, W.Z. Qian, Y.Y. Zhang, F. Wei, The road for nanomaterials industry: a review of carbon nanotube production, post-treatment, and bulk applications for composites and energy storage, Small 9 (2013) 1237.
[7] A. Holmen, H.J. Venvik, R. Myrstad, J. Zhu, D. Chen, Monolithic, microchannel and carbon nanofibers/carbon felt reactors for syngas conversion by Fischer-Tropsch synthesis, Catal. Today 216 (2013) 150.
[8] T. van Haasterecht, C.C.I. Ludding, K.P. de Jong, J.H. Bitter, Stability and activity of carbon nanofiber-supported catalysts in the aqueous phase reforming of ethylene glycol, J. Energy Chem. 22 (2013) 257.
[9] H. Yuan, Z.H. Sun, H.Y. Liu, B.S. Zhang, C.L. Chen, H.H. Wang, Z.M. Yang, J.S. Zhang, F. Wei, D.S. Su, Immobilizing carbon nanotubes on SiC foam as a monolith catalyst for oxidative dehydrogenation reactions, ChemCatChem 5 (2013) 1713.
[10] J. Zhu, A. Holmen, D. Chen, Carbon nanomaterials in catalysis: proton affinity, chemical and electronic properties, and their catalytic consequences, ChemCatChem 5 (2013) 378.
[11] X.Z. Duan, G. Qian, J.H. Zhou, X.G. Zhou, D. Chen, W.K. Yuan, Flat interface mediated synthesis of platelet carbon nanofibers on Fe nanoparticles, Catal. Today 186 (2012) 48.
[12] F.L. Lou, H.T. Zhou, T.D. Tran, M.E.M. Buan, F. Vullum-Bruer, M. Ronning, J.C. Walmsley, D. Chen, Coaxial carbon/metal oxide/aligned carbon nanotube arrays as high-performance anodes for lithium ion batteries, ChemSusChem 7 (2014) 1335.
[13] B.S. Lee, S.B. Son, K.M. Park, W.R. Yu, K.H. Oh, S.H. Lee, Anodic properties of hollow carbon nanofibers for Li-ion battery, J. Power Sources 199 (2012) 53.

[14] Z.-S. Wu, W. Ren, L. Xu, F. Li, H.-M. Cheng, Doped graphene sheets as anode materials with superhigh rate and large capacity for lithium ion batteries, ACS Nano 5 (2011) 5463.
[15] L. Bulusheva, A. Okotrub, A. Kurenya, H. Zhang, H. Zhang, X. Chen, H. Song, Electrochemical properties of nitrogen-doped carbon nanotube anode in Li-ion batteries, Carbon 49 (2011) 4013.
[16] E. Rodríguez, I. Cameán, R. García, A.B. García, Graphitized boron-doped carbon foams: performance as anodes in lithium-ion batteries, Electrochim. Acta 56 (2011) 5090.
[17] F. Su, C.K. Poh, J.S. Chen, G. Xu, D. Wang, Q. Li, J. Lin, X.W. Lou, Nitrogen-containing microporous carbon nanospheres with improved capacitive properties, Energy Environ. Sci. 4 (2011) 717.
[18] J. Masa, A. Bordoloi, M. Muhler, W. Schuhmann, W. Xia, Enhanced electrocatalytic stability of platinum nanoparticles supported on a nitrogen-doped composite of carbon nanotubes and mesoporous titania under oxygen reduction conditions, ChemSusChem 5 (2012) 523.
[19] D.S. Yu, Q. Zhang, L.M. Dai, Highly efficient metal-free growth of nitrogen-doped single-walled carbon nanotubes on plasma-etched substrates for oxygen reduction, J. Am. Chem. Soc. 132 (2010) 15127.
[20] H. Wang, C. Zhang, Z. Liu, L. Wang, P. Han, H. Xu, K. Zhang, S. Dong, J. Yao, G. Cui, Nitrogen-doped graphene nanosheets with excellent lithium storage properties, J. Mater. Chem. 21 (2011) 5430.
[21] Z. Zhou, X.P. Gao, J. Yan, D.Y. Song, M. Morinaga, Enhanced lithium absorption in single-walled carbon nanotubes by boron doping, J. Phys. Chem. B 108 (2004) 9023.
[22] X.-B. Cheng, G.-L. Tian, X.-F. Liu, J.-Q. Nie, M.-Q. Zhao, J.-Q. Huang, W. Zhu, L. Hu, Q. Zhang, F. Wei, Robust growth of herringbone carbon nanofibers on layered double hydroxide derived catalysts and their applications as anodes for Li-ion batteries, Carbon 62 (2013) 393.
[23] G.L. Tian, M.Q. Zhao, Q. Zhang, J.Q. Huang, F. Wei, Self-organization of nitrogen-doped carbon nanotubes into double-helix structures, Carbon 50 (2012) 5323.
[24] C.M. Li, M. Wei, D.G. Evans, X. Duan, Layered double hydroxide-based nanomaterials as highly efficient catalysts and adsorbents, Small 10 (2014) 4469.
[25] G. Fan, F. Li, D.G. Evans, X. Duan, Catalytic applications of layered double hydroxides: recent advances and perspectives, Chem. Soc. Rev. 43 (2014) 7040.
[26] G.L. Tian, M.Q. Zhao, B.S. Zhang, Q. Zhang, W. Zhang, J.Q. Huang, T.C. Chen, W.Z. Qian, D.S. Su, F. Wei, Monodisperse embedded nanoparticles derived from an atomic metal-dispersed precursor of layered double hydroxide for architectured carbon nanotube formation, J. Mater. Chem. A 2 (2014) 1686.
[27] M.Q. Zhao, Q. Zhang, J.Q. Huang, F. Wei, Hierarchical nanocomposites derived from nanocarbons and layered double hydroxides - properties, synthesis, and applications, Adv. Funct. Mater. 22 (2012) 675.
[28] M.Q. Zhao, Q. Zhang, J.Q. Huang, J.Q. Nie, F. Wei, Layered double hydroxides as catalysts for the efficient growth of high quality single-walled carbon nanotubes in a fluidized bed reactor, Carbon 48 (2010) 3260.
[29] Q. Zhang, W.Z. Qian, Q. Wen, Y. Liu, D.H. Wang, F. Wei, The effect of phase separation in Fe/Mg/Al/O catalysts on the synthesis of DWCNTs from methane, Carbon 45 (2007) 1645.
[30] O.Y. Podyacheva, A.N. Shmakov, A.I. Boronin, L.S. Kibis, S.V. Koscheev, E.Y. Gerasimov, Z.R. Ismagilov, A correlation between structural changes in a Ni-Cu catalyst during decomposition of ethylene/ammonia mixture and properties of nitrogen-doped carbon nanofibers, J. Energy Chem. 22 (2013) 270.
[31] O.Y. Podyacheva, Z.R. Ismagilov, A.E. Shalagina, V.A. Ushakov, A.N. Shmakov, S.V. Tsybulya, V.V. Kriventsov, A.V. Ischenko, Structural changes in a nickel-copper catalyst during growth of nitrogen-containing carbon nanofibers by ethylene/ammonia decomposition, Carbon 48 (2010) 2792.
[32] A.E. Shalagina, Z.R. Ismagilov, O.Y. Podyacheva, R.I. Kvon, V.A. Ushakov, Synthesis of nitrogen-containing carbon nanofibers by catalytic decomposition of ethylene/ammonia mixture, Carbon 45 (2007) 1808.
[33] J.Q. Huang, M.Q. Zhao, Q. Zhang, J.Q. Nie, L.D. Yao, D.S. Su, F. Wei, Efficient synthesis of aligned nitrogen-doped carbon nanotubes in a fluidized-bed reactor, Catal. Today 186 (2012) 83.
[34] Z.H. Wang, X.Q. Xiong, L. Qie, Y.H. Huang, High-performance lithium storage in nitrogen-enriched carbon nanofiber webs derived from polypyrrole, Electrochim. Acta 106 (2013) 320.
[35] D. Andre, M. Meiler, K. Steiner, C. Wimmer, T. Soczka-Guth, D.U. Sauer, Characterization of high-power lithium-ion batteries by electrochemical impedance spectroscopy. I. Experimental investigation, J. Power Sources 196 (2011) 5334.
[36] W. Ren, D.J. Li, H. Liu, R. Mi, Y. Zhang, L. Dong, L. Dong, Lithium storage performance of carbon nanotubes with different nitrogen contents as anodes in lithium ions batteries, Electrochim. Acta 105 (2013) 75.
[37] L. Qie, W.M. Chen, Z.H. Wang, Q.G. Shao, X. Li, L.X. Yuan, X.L. Hu, W.X. Zhang, Y.H. Huang, Nitrogen-doped porous carbon nanofiber webs as anodes for lithium ion batteries with a superhigh capacity and rate capability, Adv. Mater. 24 (2012) 2047.
[38] C. Tang, Q. Zhang, M.Q. Zhao, J.Q. Huang, X.B. Cheng, G.L. Tian, H.J. Peng, F. Wei, Nitrogen-doped aligned carbon nanotube/graphene sandwiches: facile catalytic growth on bifunctional natural catalysts and their applications as scaffolds for high-rate lithium-sulfur batteries, Adv. Mater. 26 (2014) 6100.
[39] H.Q. Wang, Z.B. Zhao, M. Chen, N. Xiao, B.B. Li, J.S. Qiu, Nitrogen-doped mesoporous carbon nanosheets from coal tar as high performance anode materials for lithium ion batteries, New Carbon Mater. 29 (2014) 280.
[40] J.J. Jiang, X.L. Tang, R. Wu, H.Q. Lin, M.Z. Qu, Electrochemical performance of polygonized carbon nanofibers as anode materials for lithium-ion batteries, Particuology 11 (2013) 401.
[41] X.F. Li, J. Liu, Y. Zhang, Y.L. Li, H. Liu, X.B. Meng, J.L. Yang, D.S. Geng, D.N. Wang, R.Y. Li, X.L. Sun, High concentration nitrogen doped carbon nanotube anodes with superior Li^+ storage performance for lithium rechargeable battery application, J. Power Sources 197 (2012) 238.
[42] C.Y. He, R.H. Wang, H.G. Fu, P.K. Shen, Nitrogen-self-doped graphene as a high capacity anode material for lithium-ion batteries, J. Mater. Chem. A 1 (2013) 14586.
[43] C.C. Ma, X.H. Shao, D.P. Cao, Nitrogen-doped graphene nanosheets as anode materials for lithium ion batteries: a first-principles study, J. Mater. Chem. 22 (2012) 8911.
[44] H.J. Peng, T.Z. Hou, Q. Zhang, J.Q. Huang, X.B. Cheng, M.Q. Guo, Z. Yuan, L.Y. He, F. Wei, Strongly coupled interfaces between heterogeneous carbon host and sulfur-containing guest for highly-stable lithium-sulfur batteries: mechanistic insight into capacity degradation, Adv. Mater. Interfaces 1 (2014) 1400227.
[45] V.R. Stamenkovic, B.S. Mun, M. Arenz, K.J.J. Mayrhofer, C.A. Lucas, G. Wang, P.N. Ross, N.M. Markovic, Trends in electrocatalysis on extended and nanoscale Pt-bimetallic alloy surfaces, Nat. Mater. 6 (2007) 241.
[46] A. Morozan, B. Jousselme, S. Palacin, Low-platinum and platinum-free catalysts for the oxygen reduction reaction at fuel cell cathodes, Energy Environ. Sci. 4 (2011) 1238.
[47] K.P. Gong, F. Du, Z.H. Xia, M. Durstock, L.M. Dai, Nitrogen-doped carbon nanotube arrays with high electrocatalytic activity for oxygen reduction, Science 323 (2009) 760.
[48] G.L. Tian, M.Q. Zhao, D.S. Yu, X.Y. Kong, J.Q. Huang, Q. Zhang, F. Wei, Nitrogen-doped graphene/carbon nanotube hybrids: in situ formation on bifunctional catalysts and their superior electrocatalytic activity for oxygen evolution/reduction reaction, Small 10 (2014) 2251.
[49] Z. Chen, D. Higgins, Z.W. Chen, Nitrogen doped carbon nanotubes and their impact on the oxygen reduction reaction in fuel cells, Carbon 48 (2010) 3057.
[50] W. Ai, Z.M. Luo, J. Jiang, J.H. Zhu, Z.Z. Du, Z.X. Fan, L.H. Xie, H. Zhang, W. Huang, T. Yu, Nitrogen and sulfur codoped graphene: multifunctional electrode materials for high-performance Li-ion batteries and oxygen reduction reaction, Adv. Mater. 26 (2014) 6186.
[51] F.L. Meng, L. Li, Z. Wu, H.X. Zhong, J.C. Li, J.M. Yan, Facile preparation of N-doped carbon nanofiber aerogels from bacterial cellulose as an efficient oxygen reduction reaction electrocatalyst, Chin. J. Catal. 35 (2014) 877.
[52] D.S. Yu, L. Wei, W.C. Jiang, H. Wang, B. Sun, Q. Zhang, K.L. Goh, R.M. Si, Y. Chen, Nitrogen doped holey graphene as an efficient metal-free multifunctional electrochemical catalyst for hydrazine oxidation and oxygen reduction, Nanoscale 5 (2013) 3457.
[53] A.Q. Zhao, J. Masa, W. Schuhmann, W. Xia, Activation and stabilization of nitrogen-doped carbon nanotubes as electrocatalysts in the oxygen reduction reaction at strongly alkaline conditions, J. Phys. Chem. C 117 (2013) 24283.
[54] D.S. Yu, K.L. Goh, L. Wei, H. Wang, Q. Zhang, W.C. Jiang, R.M. Si, Y. Chen, Multifunctional nitrogen-rich "brick-and-mortar" carbon as high performance supercapacitor electrodes and oxygen reduction electrocatalysts, J. Mater. Chem. A 1 (2013) 11061.
[55] G.-L. Tian, Q. Zhang, B. Zhang, Y.-G. Jin, J.-Q. Huang, D.S. Su, F. Wei, Toward full exposure of "active sites": nanocarbon electrocatalyst with surface enriched nitrogen for superior oxygen reduction and evolution reactivity, Adv. Funct. Mater. 24 (2014) 5956.